Supplementary Information (SI) for Journal of Materials Chemistry A.

Supporting Information

Synergetic passivation of PbS colloidal quantum dots by bulk heterojunction-type interlayers enables >14% solar cell efficiency

Ching-Hsuan Cheng,[a†] Sheng-Fu Wang,[a†] Chieh-Ming Hung,[a†] Bo-Han Chen,[c] Ying-Yi Tsai,[a] Ching-Yuan Chu,[a] Chen-Yu Lin,[a] I-Chih Ni,[d] Chen-Sheng Lo,[b] Chih-I Wu,[d] Shang-Da Yang,[c] Hsieh-Chih Chen*[b] and Pi-Tai Chou*[a]

[a]Department of Chemistry
Center for Emerging Materials and Advanced Devices
National Taiwan University
Taipei 106319, Taiwan
E-mail: chop@ntu.edu.tw

[b]Department of Chemistry
Fu Jen Catholic University
New Taipei City 242062, Taiwan
E-mail: 158266@mail.fju.edu.tw

[c]Institute of Photonics Technologies
National Tsing Hua University
Hsinchu 300044, Taiwan

[d]Graduate Institute of Photonics and Optoelectronics
National Taiwan University,
Taipei 106319, Taiwan

[†] These authors contributed equally.

Experimental

Materials and chemicals:

Lead acetate dihydrate ($Pb(Ac)_2\cdot 2H_2O$, 99%), octadecene (ODE, 95%), oleic acid (OA, 90%), ammonium acetate (NH_4Ac, 98%), butylamine (99.5%), ethanolamine (C_2H_7NO, 98%), HPLC-grade dry isopropanol (IPA), chloroform (99%), and hexane (97%) were purchased from Sigma-Aldrich. Lead iodide (PbI_2, 99%), lead bromide ($PbBr_2$, 99.998%), zinc acetate dihydrate ($Zn(Ac)_2\cdot 2H_2O$, 98%), indium chloride ($InCl_3$, 99.995%), 2-methoxyethanol (2-ME, anhydrous, 99%), toluene (99.85%), and dimethylformamide (DMF, anhydrous, 99.8%) were obtained from Thermo Scientific. Hexamethyldisilithiane [$(TMS)_2S$] was purchased from TCI. Acetone was obtained from DUKSAN, ethanol (EtOH) from Honeywell, and acetonitrile from Acros. PTB7-Th and $PC_{71}BM$ (99%) were purchased from Lumtec.

PbS colloidal quantum dot synthesis:

The size distribution of PbS colloidal quantum dots (CQDs) was tuned by adjusting the molar ratio between lead acetate and oleic acid (OA), which improved the homogeneity of the PbS active layer and reduced inter-dot spacing, thereby facilitating efficient carrier transport in solar cell devices. A 0.395 M precursor solution was prepared using lead acetate trihydrate, OA, and octadecene (ODE) with a molar ratio of $OA:Pb(Ac)_2\cdot 3H_2O:(TMS)_2S = 5:2:1$. Specifically, 1.9 g of $Pb(Ac)_2\cdot 3H_2O$, 3.5 g of OA, and 10 g of ODE were loaded into a three-neck round-bottom flask and degassed at 100 °C under vacuum for 2 h to generate lead oleate (Pb–OA). The mixture was cooled to 90 °C, followed by rapid injection of 525 μL of bis(trimethylsilyl)sulfide ($(TMS)_2S$) under vigorous stirring in a nitrogen atmosphere. After a 3 min reaction at 90 °C, the solution was quenched with twice the volume of anhydrous isopropanol, centrifuged at 8000 rpm for 5 min, redispersed in anhydrous hexane, and reprecipitated with acetone. The resulting PbS CQDs were collected by centrifugation, vacuum-dried for 2 h, and stored in a nitrogen-filled glovebox for up to 3 weeks. The typical yield of PbS–OA CQDs was ~1.5 g.

Synthesis of IZO films:

An indium-doped zinc oxide (IZO) precursor solution was prepared by dissolving 0.2 g of zinc acetate dihydrate and 60 μL of ethanolamine in 2 mL of 2-methoxyethanol, followed by the addition of indium chloride ($InCl_3$) at a 1 mol% doping ratio relative to Zn^{2+}. The solution was stirred at room temperature for 24 h to obtain a clear and homogeneous precursor. ITO-coated glass substrates were sequentially cleaned by ultrasonication in detergent, deionized water, acetone, and isopropanol, then dried overnight in an oven. Prior to deposition, the substrates were treated with UV–ozone for 20 min to improve surface wettability and remove residual organic contaminants. The IZO precursor was then spin-coated at 3000 rpm for 40 s and annealed in air at 150 °C for 30 min to induce film crystallization.

Ligand exchange of PbS CQDs for active layer:

Prior to device fabrication, the as-synthesized PbS–OA CQDs underwent a solution-phase ligand exchange. Solution A was prepared by dispersing PbS–OA CQDs in hexane, while Solution B consisted of 0.1 M PbI_2, 0.04 M $PbBr_2$, and 0.04 M NH_4Ac dissolved in DMF. Solution A was rapidly injected into Solution B and stirred vigorously for 4 min. The resulting biphasic mixture was centrifuged at 4000 rpm for 3 min to remove the colorless hexane supernatant, followed by three additional hexane washes. The exchanged CQDs were precipitated with toluene, centrifuged at 8000 rpm for 5 min, washed with ethanol, and vacuum-dried for 20 min to yield PbS–I,Br CQDs. Unlike conventional layer-by-layer (LBL) ligand exchange, this solution-phase approach simplifies processing and mitigates defect formation, thereby improving device efficiency and operational stability. The resulting CQDs possessed mixed halide-terminated surfaces (I^-, Br^-), forming a double ionic shell structure comprising PbX_3^-, NH_4^+, and PbX^+. These CQDs exhibited good dispersibility in polar solvents such as butylamine due to steric repulsion from the butyl chains; however, the limited polarity of butylamine caused poor long-term colloidal stability and aggregation. To address this, a solvent mixture (Solution C) of butylamine:DMF = 2:1 was employed to modulate polarity and enhance colloidal stability. For device fabrication, 320 mg of PbS CQDs were dispersed in 1 mL of Solution C, stirred at 300 rpm for 1 min, filtered through a 0.22 μm PTFE syringe filter, and immediately used for active-layer deposition.

Device fabrication of PbS CQD solar cells:

PbS CQD solar cells were fabricated in a conventional n–i–p architecture. ITO-coated glass substrates were cleaned as described above, treated with UV–ozone for 20 min, and coated with an indium-doped zinc oxide (IZO) electron transport layer by spin coating at 3000 rpm for 40 s, followed by annealing at 150 °C for 30 min. Subsequently, a PbS CQD solution (320 mg mL^{-1}) was spin-coated at 2500 rpm for 40 s and thermally annealed at 90 °C for 1 min to remove residual solvents, followed by vacuum drying for 3 min. Hole-transporting layers (HTLs) (~30 nm) were deposited using a "spin-then-drop" method from chloroform-based solutions of PTB7-Th:$PC_{71}BM$ (3:1, 10 mg mL^{-1}), PTB7-Th:BTPV-4F:$PC_{71}BM$ (3:2:0.7, 5 mg mL^{-1}), and PTB7-Th:BATPV-4F:$PC_{71}BM$ (3:2:0.7, 5 mg mL^{-1}) at 2750 rpm. The resulting films were dried under ambient conditions for 30 min, followed by solvent vapor annealing (SVA) with chlorobenzene and chloroform to promote molecular self-assembly within the HTL. Finally, 10 nm of MoO_3 and 100 nm of Ag were thermally evaporated as top electrodes to complete the device.

Characterization:

Current density–voltage (*J–V*) curves were recorded under AM 1.5G illumination (100 mW cm^{-2}) using a Newport Sol3A Class AAA solar simulator, and independently verified with a 300 W AM 1.5G source. Light intensity was calibrated with a mono-silicon detector equipped with a KG-5 visible filter (calibrated by NREL) to minimize spectral mismatch. Monochromatic incident photon-to-electron conversion efficiency (IPCE) spectra were measured under short-circuit conditions using a lock-in amplifier with a current preamplifier (PV Measurement). Devices were illuminated with monochromatic light from a xenon lamp coupled to a monochromator at ~30 μW intensity. A calibrated mono-silicon photodiode with a known spectral response served as the reference. X-ray photoelectron spectroscopy (XPS, ULVAC-PHI, Japan) was employed to probe the chemical composition and surface interactions of perovskite films. Morphological characterization was performed by scanning electron microscopy (SEM, Hitachi S-4800). Grazing-incidence wide-angle X-ray scattering (GIWAXS) measurements were conducted at beamline BL23A1 of the National Synchrotron Radiation Research Center (NSRRC, Taiwan), using a Mar345 CCD detector (40 mm diameter). The scattering vector (q), d-spacing ($d = 2\pi/q$), and scattering angles were calibrated with silver behenate. Optical absorption spectra were collected using a Hitachi UH-5700 spectrophotometer, while steady-state photoluminescence (PL) spectra were recorded with an Edinburgh FLS980 system. Electrochemical impedance spectroscopy (EIS) was performed using a Metrohm Autolab under ambient conditions at 0.9 V in the dark, with data analyzed by NOVA 2.0 software. Space-charge-limited current (SCLC) measurements were carried out under dark conditions using a Keithley 2400 SourceMeter. Hole-only devices were fabricated using the structure ITO/MoO_3/BHJ layer/MoO_3/Al, where the BHJ layer consisted of PTB7-Th:$PC_{71}BM$, PTB7-Th:BTPV-4F:$PC_{71}BM$, or PTB7-Th:BATPV-4F:$PC_{71}BM$. The use of MoO_3 as both the bottom and top interfacial layers ensures selective hole injection/extraction and suppresses electron transport, thereby enabling reliable SCLC characterization. The *J–V* curves were recorded under dark conditions over an applied bias range of 1.5–2.0 V, where the devices enter the trap-free SCLC regime. For analysis, the *J–V* characteristics were replotted on a log(*J*)–log(*V*) scale to identify the ohmic region (slope ≈ 1) and the SCLC region (slope ≈

2). The V_{TFL} was extracted from the intersection point between linear fits to these two regions. Using V_{TFL}, the trap density (N_{t}) was calculated according to:

$$N_{\mathrm{t}} = \frac{2\varepsilon_{\mathrm{r}}\varepsilon_0 V_{\mathrm{TFL}}}{qL^2} \qquad (1)$$

where ε_{r} is the relative permittivity of the BHJ layer, ε_0 is the vacuum permittivity, q is the elementary charge, and L is the measured thickness of the BHJ film. In the trap-free SCLC region, the current density follows the Mott–Gurney law:

$$J = \frac{9}{8}\varepsilon_r\varepsilon_0\mu\frac{V^2}{L^3} \qquad (2)$$

which was used to extract the hole mobility (μ) for each BHJ composition via linear fitting of the J vs. V^2 dependence. Cyclic voltammetry (CV) and differential pulse voltammetry (DPV) analyses were conducted to verify the intrinsic electronic properties of zwitterion derivatives. An Ag/Ag$^+$ (0.01 M $AgNO_3$) electrode was used as the reference electrode. The oxidation potentials were measured using a platinum electrode in dimethyl sulfoxide as the working electrode, with 0.1 M $[NBu_4]^+PF_6^-$ as the electrolyte and platinum wire as the counter electrode. The potentials were further referenced to the ferrocenium/ferrocene (Fc$^+$/Fc) couple ($E_{ox}^{Fc} = 0.18$ V). The HOMO energy levels (E_{HOMO}) were calculated using the equation $E_{\mathrm{HOMO}} = -(E_{\mathrm{ox}} - E_{\mathrm{FC}} + 4.8)$ eV. High-resolution field desorption (HRFD) mass spectra were recorded on a JEOL AccuTOF GCX instrument. ^{1}H NMR (400 MHz) and ^{13}C NMR (101 MHz) spectra were acquired using Bruker AVIII HD 400 MHz and Agilent Unity+ 400 MHz spectrometers. Chemical shifts are reported in ppm relative to residual solvent signals.

Setup of light source and transient absorption spectroscopy:

The details are summarized as follows. The measurements were conducted using a commercial Yb:KGW laser system (Pharos, Light Conversion) with a central wavelength of 1030 nm, an average power of 2.5 W, a repetition rate of 3.125 kHz, a pulse energy of 800 μJ, and a pulse duration of 190 fs. Two identical pulses were generated using a low-GDD 50/50 beam splitter and then passed through our designed nonlinear compressor, employing a technique known as multiple plate compression (MPC). A high-pass filter with a cut-off wavelength of 980 nm was applied for this experiment. Pulse compression was achieved with 8 chirped mirror bounces (Ultrafast Innovation) to remove the material dispersion introduced by the optics before the sample. The pump pulse was modulated by a laser-triggered mechanical chopper at half the laser repetition rate (1.5625 kHz). A broadband half-wave plate and wire-grid polarizer were employed to precisely control the excitation power and prevent any nonlinear effects. The delay time of the probe pulse relative to the pump pulse was adjusted using a linear translation stage

(DL325, Newport) with a delay range of up to approximately 2.2 ns. The pump and probe beams were focused on the sample in a noncollinear manner with a cross-angle of 5°. Different focusing conditions were chosen for the pump and probe pulses to ensure that the focused pump spot size (~67.7 μm) was slightly larger than the focused probe spot size (~27.3 μm), ensuring uniform excitation of the probed region. After passing through the sample, the transmitted probe pulse was spatially separated and guided into our designed spectrometer. The spectrometer included a high-speed linear array camera (Glaz Linescan-I-Gen2, Synertronic with S12198-512Q CMOS, Hamamatsu) to capture each probe pulse. Since the pump pulses were modulated at half the repetition rate, the spectral difference between every two probe shots (one exposed to the pump and the other not) provided the Δ*T*/*T* signal.

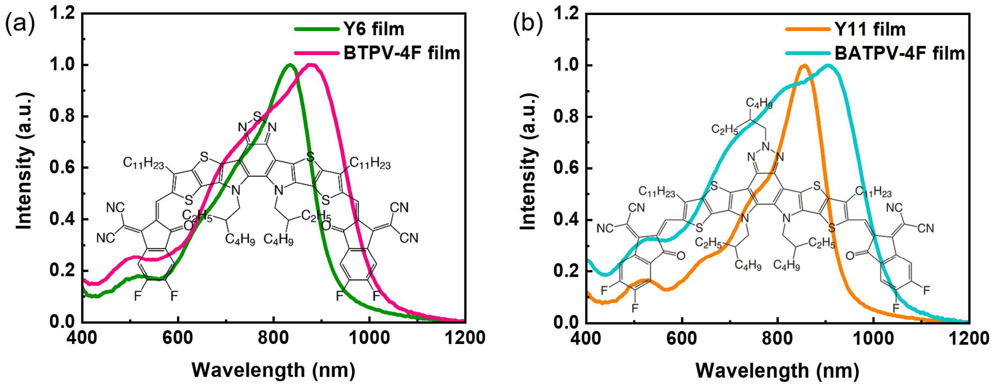

Fig. S1. UV–vis absorption spectra of (a) Y6 and BTPV-4F, and (b) Y11 and BATPV-4F thin films, together with the corresponding molecular structures of Y6 and Y11.

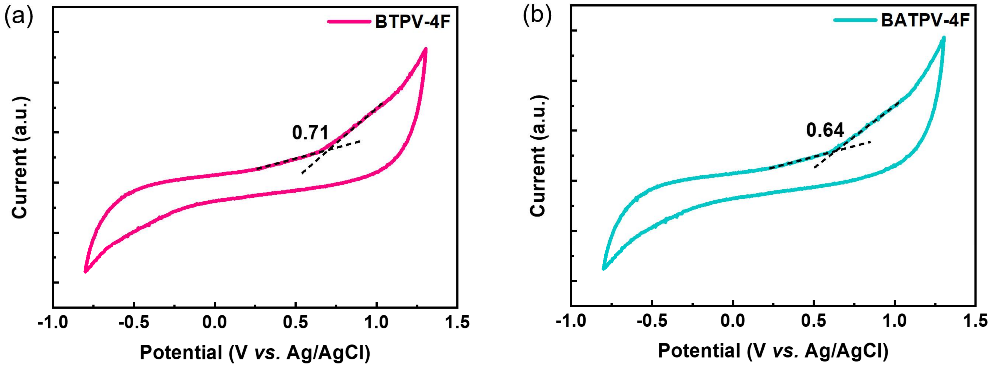

Fig. S2. HOMO energy levels of BTPV-4F and BATPV-4F determined from CV measurements.

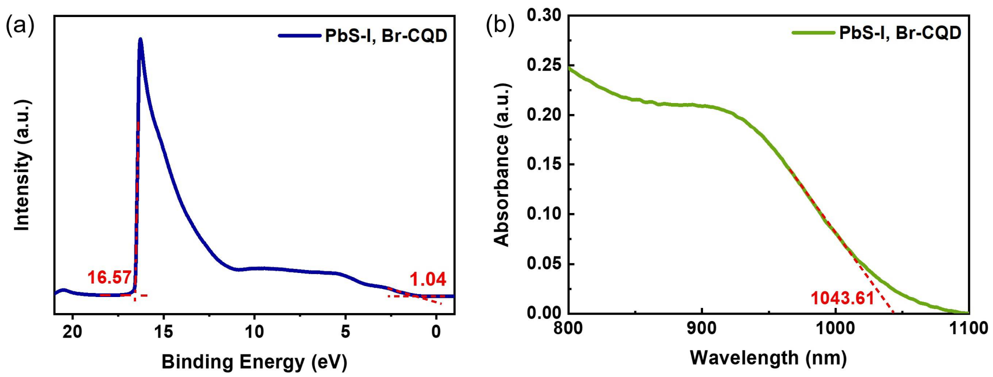

Fig. S3. Determination of the valence band maximum (VBM) and conduction band minimum (CBM) of PbS CQDs by ultraviolet photoelectron spectroscopy (UPS) combined with optical absorption edge analysis.

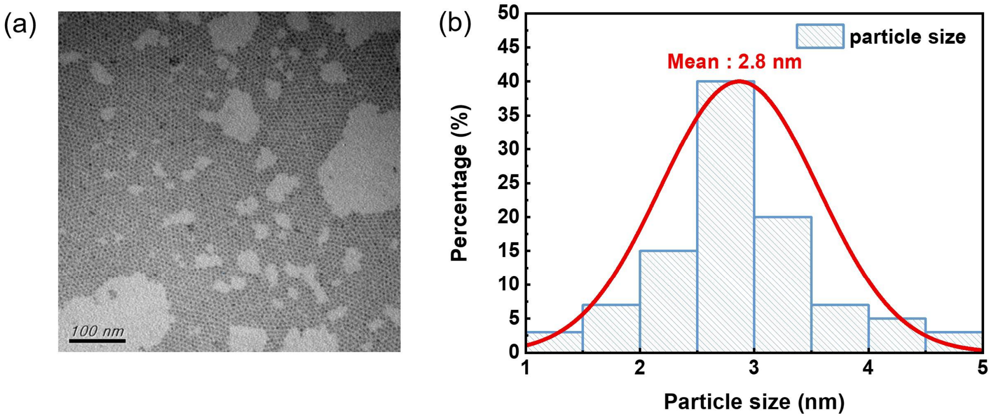

Fig. S4. (a) TEM image of PbS CQDs and (b) corresponding particle size distribution statistics.

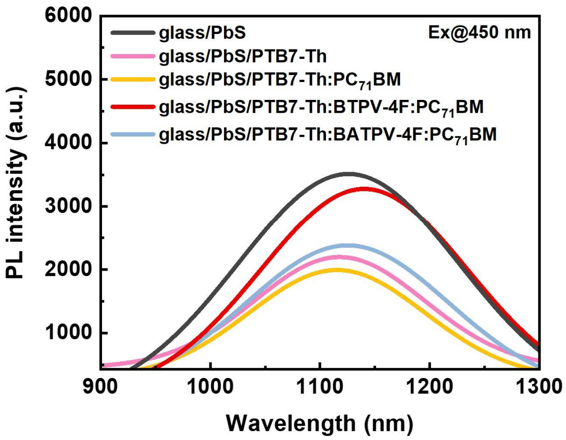

Fig. S5. Photoluminescence spectra of PbS films with and without different BHJ-HTLs under 450 nm excitation.

A pristine glass/PbS film shows the highest emission intensity with a peak around 1120 nm. Coating PbS with PTB7-Th or with the PTB7-Th:$PC_{71}BM$ BHJ strongly quenches the PL, indicating efficient interfacial charge transfer but also the introduction of additional nonradiative channels at the CQD/organic interface. When BTPV-4F or BATPV-4F is incorporated into the BHJ, the PbS PL intensity partially recovers relative to the PTB7-Th:$PC_{71}BM$ case. This recovery is not due to emission from the NFAs themselves but reflects a real increase in the radiative fraction of recombination within PbS. XPS shows that the NFAs introduce additional Pb–S and Pb–O coordination, and KPFM reveals a more uniform interfacial potential, both of which reduce the density and activity of surface traps. Combined with the ps-TA spectra evidence of longer τ_{decay}, these results support a picture in which the NFAs simultaneously maintain efficient charge transfer while mitigating the nonradiative loss channels that were introduced when only PTB7-Th:$PC_{71}BM$ is used.

In addition, among the examined BHJ-HTLs, the BTPV-4F ternary film exhibits the tightest π–π stacking and the longest coherence length in GIWAXS, as well as the most pronounced XPS signatures of Pb–S coordination and the narrowest GSB linewidth in ps-TA spectra. These features indicate that BTPV-4F forms a highly ordered, polarizable interfacial layer that enhances dielectric screening around the PbS nanocrystals and reduces energetic disorder at the band edge. Stronger dielectric screening lowers the exciton binding energy and relaxes the effective quantum confinement, which shifts the band-edge emission to slightly lower energy (longer wavelength). At the same time, more effective trap passivation suppresses higher-energy trap-mediated recombination pathways, so that the PL spectrum is dominated by cleaner band-edge emission. The net result is the modest but distinct red shift observed for the PbS/PTB7-Th:BTPV-4F:$PC_{71}BM$ stack compared to pristine PbS and the other BHJ configurations.

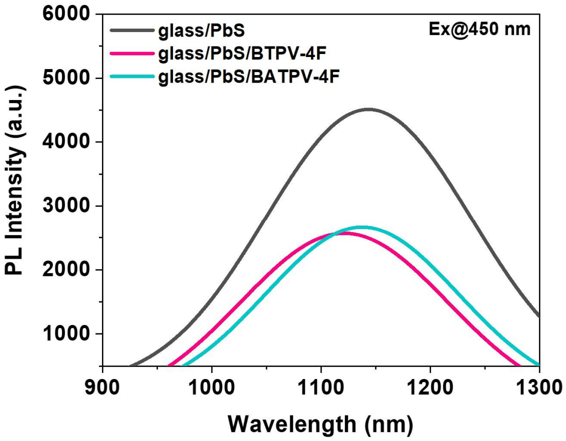

Fig. S6. Photoluminescence spectra of PbS films with and without BTPV-4F and BATPV-4F measured under 450 nm excitation.

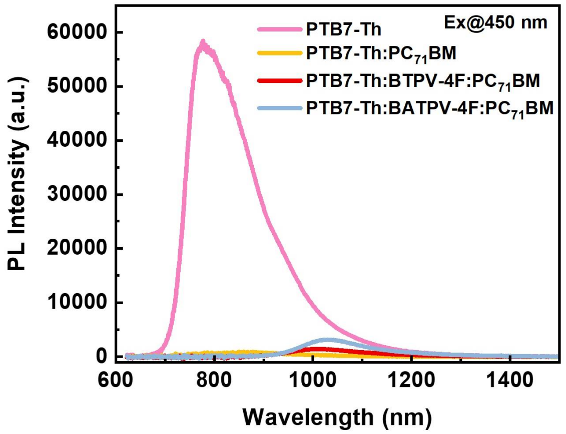

Fig. S7. Photoluminescence spectra of PTB7-Th, PTB7-Th:$PC_{71}BM$, PTB7-Th: BTPV-4F:$PC_{71}BM$, and PTB7-Th:BATPV-4F:$PC_{71}BM$ films under 450 nm excitation.

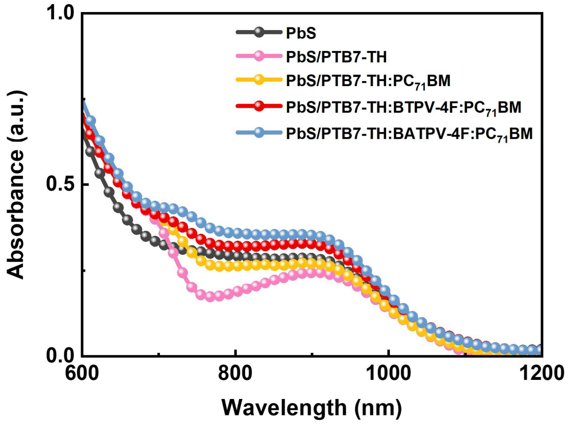

Fig. S8. UV−vis absorption spectra of PbS films with and without different BHJ-HTLs.

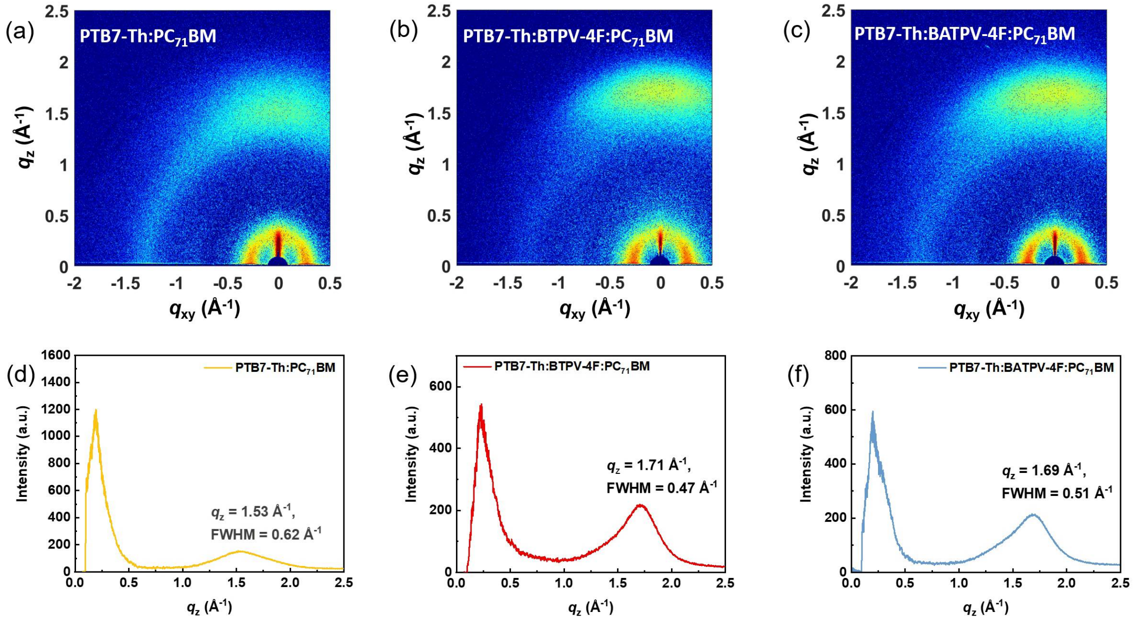

Fig. S9. 2D GIWAXS patterns of (a) PTB7-Th:PC$_{71}$BM, (b) PTB7-Th:BTPV-4F:PC$_{71}$BM, and (c) PTB7-Th:BATPV-4F:PC$_{71}$BM blend films. Corresponding out-of-plane line-cut profiles of (d) PTB7-Th:PC$_{71}$BM, (e) PTB7-Th:BTPV-4F:PC$_{71}$BM, and (f) PTB7-Th:BATPV-4F:PC$_{71}$BM films.

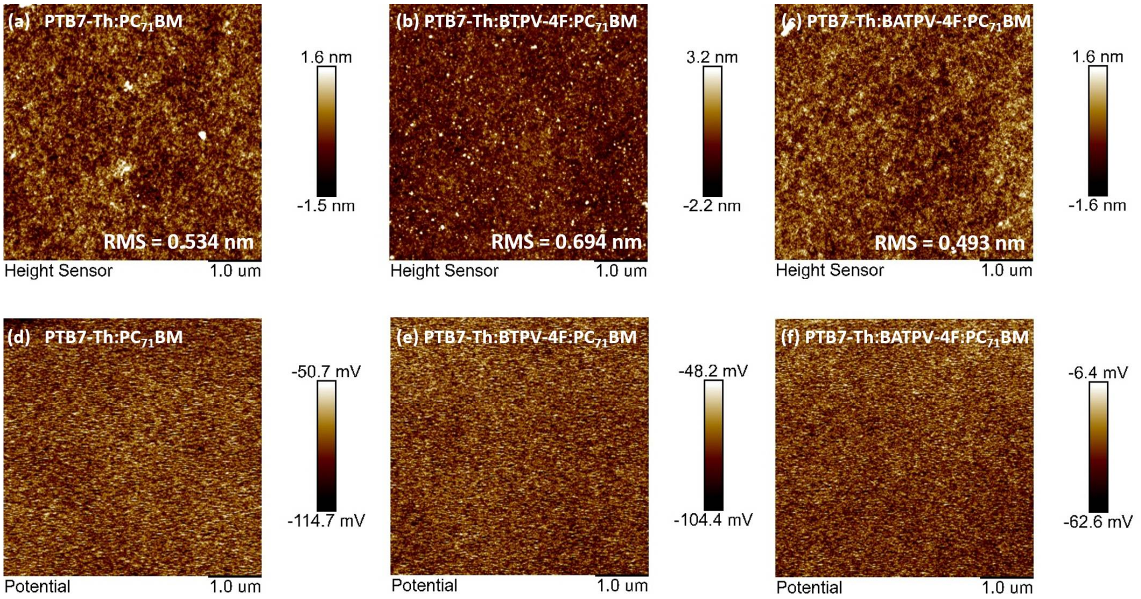

Fig. S10. Morphology characterization of (a–c) TM-AFM topography and (d–f) KPFM images of PTB7-Th:PC$_{71}$BM (panels a and d) , PTB7-Th:BTPV-4F:PC$_{71}$BM (panels b and e) , and PTB7-Th:BATPV-4F:PC$_{71}$BM (panels c and f) blend films.

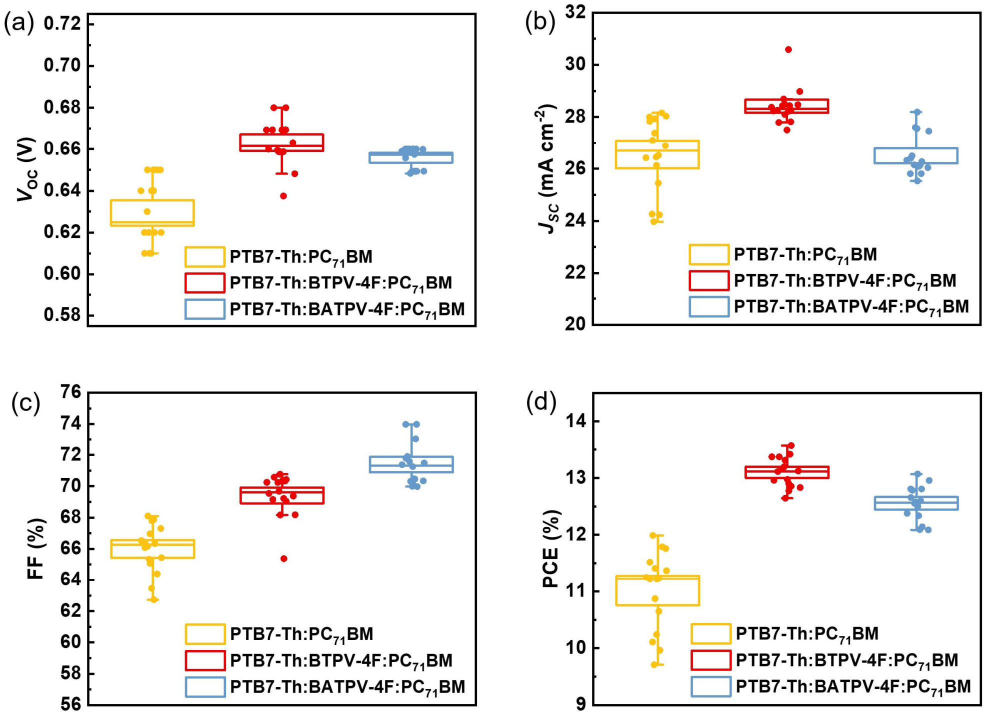

Fig. S11. Box plots of (a) V_{OC}, (b) J_{SC}, (c) FF, and (d) PCE values for devices fabricated with different BHJ-HTLs.

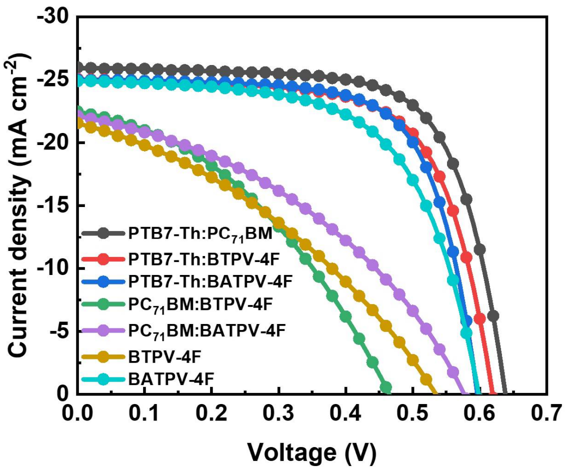

Fig. S12. *J–V* curves of PbS CQD solar cells with various BHJ-HTLs.

Devices employing NFA-only HTLs (BTPV-4F or BATPV-4F) showed poor photovoltaic performance, with PCE values of 4.10% for BTPV-4F and 9.19% for BATPV-4F, together with low FF and V_{OC} values well below those of the ternary devices. These results demonstrate that the NFAs alone do not provide continuous and efficient hole-transport pathways, despite their favorable energy levels and interfacial coordination ability.

Similarly, devices using $PC_{71}BM$:NFA binary HTLs also performed poorly, yielding efficiencies of only 4.06–5.03%, confirming that $PC_{71}BM$ does not contribute to hole transport and cannot form an effective percolation network with the NFA. In contrast, PTB7-Th:NFA binary HTLs produced markedly improved performance, with PCE values of 10.41% for PTB7-Th:BTPV-4F and 10.28% for PTB7-Th:BATPV-4F. These values are significantly higher than those of the NFA-only or $PC_{71}BM$:NFA devices and reveal that PTB7-Th is the primary hole-transport medium within the blend.

These control experiments unambiguously establish that the ternary PTB7-Th:NFA: $PC_{71}BM$ HTL operates through a cooperative mechanism in which PTB7-Th supplies the dominant hole-transport pathways, the NFA provides interfacial defect passivation and improves energetic uniformity at the CQD interface, and $PC_{71}BM$ contributes to morphological stabilization of the nanoscale blend. The sharply reduced device performance observed when any one of these components is removed confirms that all three materials play distinct and nonredundant roles, and that the superior performance of the ternary HTLs arises from their synergistic combination rather than from the behavior of any individual component.

Table S1. Photovoltaic parameters of other champion PbS CQD solar cells.

Other BHJ-HTLs [5 mg mL^{-1}]	V_{OC} [V]	J_{SC} [mA cm^{-2}]	FF [%]	PCE [%]
PTB7-Th:$PC_{71}BM$	0.63	25.95	70.22	11.48
PTB7-Th:BTPV-4F	0.61	25.04	68.14	10.41
BTPV-4F	0.53	21.53	35.93	4.10
$PC_{71}BM$:BTPV-4F	0.46	22.47	39.25	4.06
PTB7-Th:BATPV-4F	0.59	25.03	69.64	10.28
BATPV-4F	0.59	24.90	62.55	9.19
$PC_{71}BM$:BATPV-4F	0.57	22.13	39.88	5.03

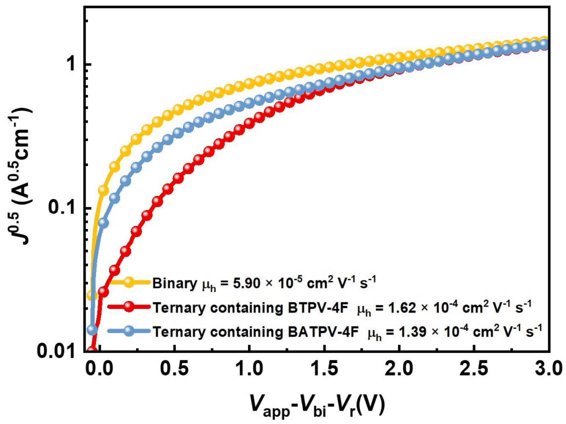

Fig. S13. Determination of hole mobilities from dark current density measurements for optimized PTB7-Th:$PC_{71}BM$, PTB7-Th:BTPV-4F:$PC_{71}BM$, and PTB7-Th:BATPV-4F:$PC_{71}BM$ hole-only devices.

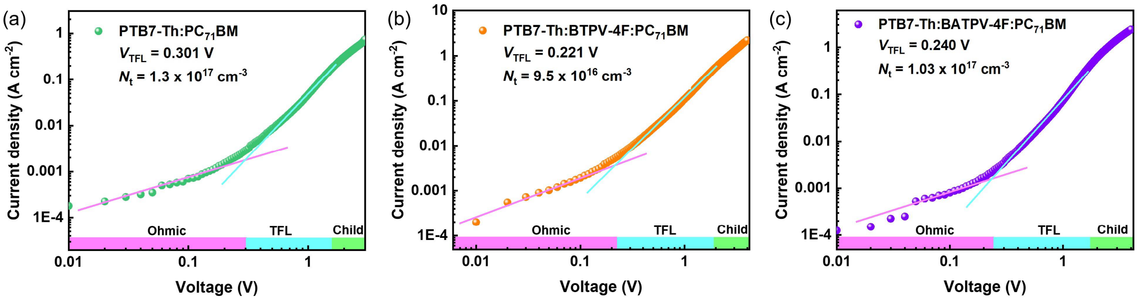

Fig. S14. SCLC curves of (a) PTB7-Th:$PC_{71}BM$, (b) PTB7-Th:BTPV-4F:$PC_{71}BM$, and (c) PTB7-Th:BATPV-4F:$PC_{71}BM$ modified PbS CQDs based on hole-only devices.

The PTB7-Th:$PC_{71}BM$ binary HTL exhibits a V_{TFL} of 0.301 V, corresponding to a trap density of approximately 1.3 × 10^{17} cm^{-3}. Incorporating BTPV-4F reduces V_{TFL} to 0.221 V, yielding a trap density of 9.5 × 10^{16} cm^{-3}, while BATPV-4F results in a V_{TFL} of 0.240 V, with a trap density of 1.03 × 10^{17} cm^{-3}. These values indicate that both NFA-containing ternary BHJ layers possess substantially lower trap densities than the PTB7-Th:$PC_{71}BM$ reference, consistent with the reduced interfacial energetic disorder and enhanced passivation effects.

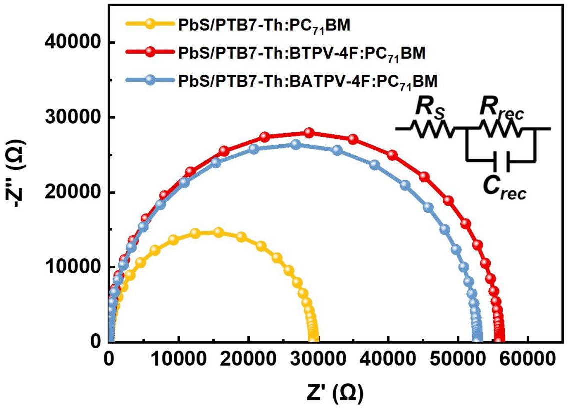

Fig. S15. EIS plots of PbS CQD solar cells fabricated with different BHJ-HTLs. Inset: the corresponding equivalent circuit.

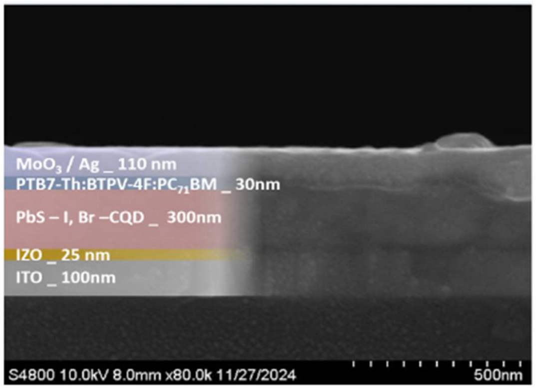

Fig. S16. Cross-sectional SEM image of the PbS CQD device with PTB7-Th:BTPV-4F:PC$_{71}$BM BHJ-HTL modification.

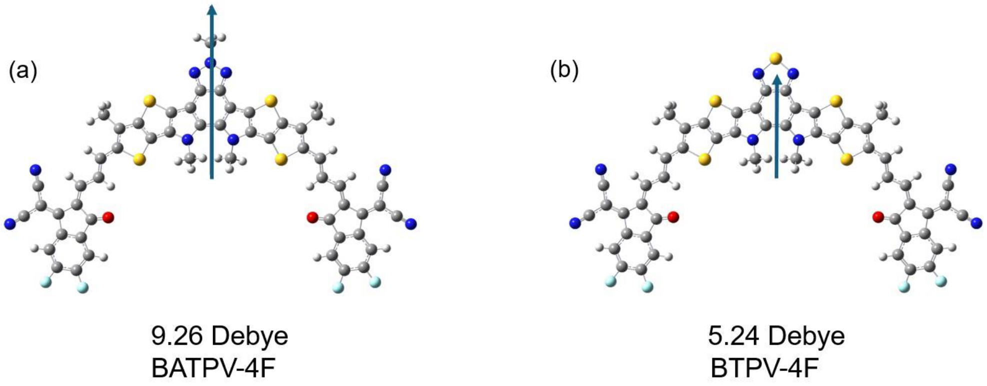

Fig. S17. Top views of the optimized geometries of BATPV-4F and BTPV-4F molecules calculated at the B3LYP/6-311G(d,p) level. The direction and magnitude of the dipole moment are indicated by arrows.

The calculations confirm that both BATPV-4F and BTPV-4F adopt highly planar A–DA′D–A conjugated backbones. The dihedral angles along the fused-ring cores and adjacent π-bridges remain below approximately 10°, indicating strong backbone coplanarity. This intrinsic planarity is characteristic of Y6/Y11-derived fused acceptors and is fully consistent with our GIWAXS results, which show reduced π–π stacking distances and increased coherence lengths upon incorporation of these NFAs. Such structural rigidity rationalizes the enhanced molecular ordering and more efficient hole-transport pathways observed in the BHJ-HTLs.

The DFT calculations also quantify both the magnitude and the correct direction of the molecular dipoles. BATPV-4F exhibits a dipole moment of 9.26 Debye, whereas BTPV-4F shows a smaller dipole moment of 5.24 Debye. As clearly indicated by the dipole arrows in Fig. S17, the dipole vectors lie within the molecular plane. The dipole arises from the overall intramolecular charge asymmetry of the fused A–DA′D–A framework, reflecting the combined contributions of the heteroatom-rich central core, asymmetric side-chain substitution, and electron-withdrawing end groups. The larger dipole moment of BATPV-4F explains its stronger electrostatic perturbation of the interface and its more pronounced Pb–O interaction signature in O 1s XPS, whereas BTPV-4F, despite its smaller dipole moment, benefits from a higher density of sulfur coordination sites and more favorable π–π packing, leading to stronger Pb–S passivation and ultimately superior device performance.

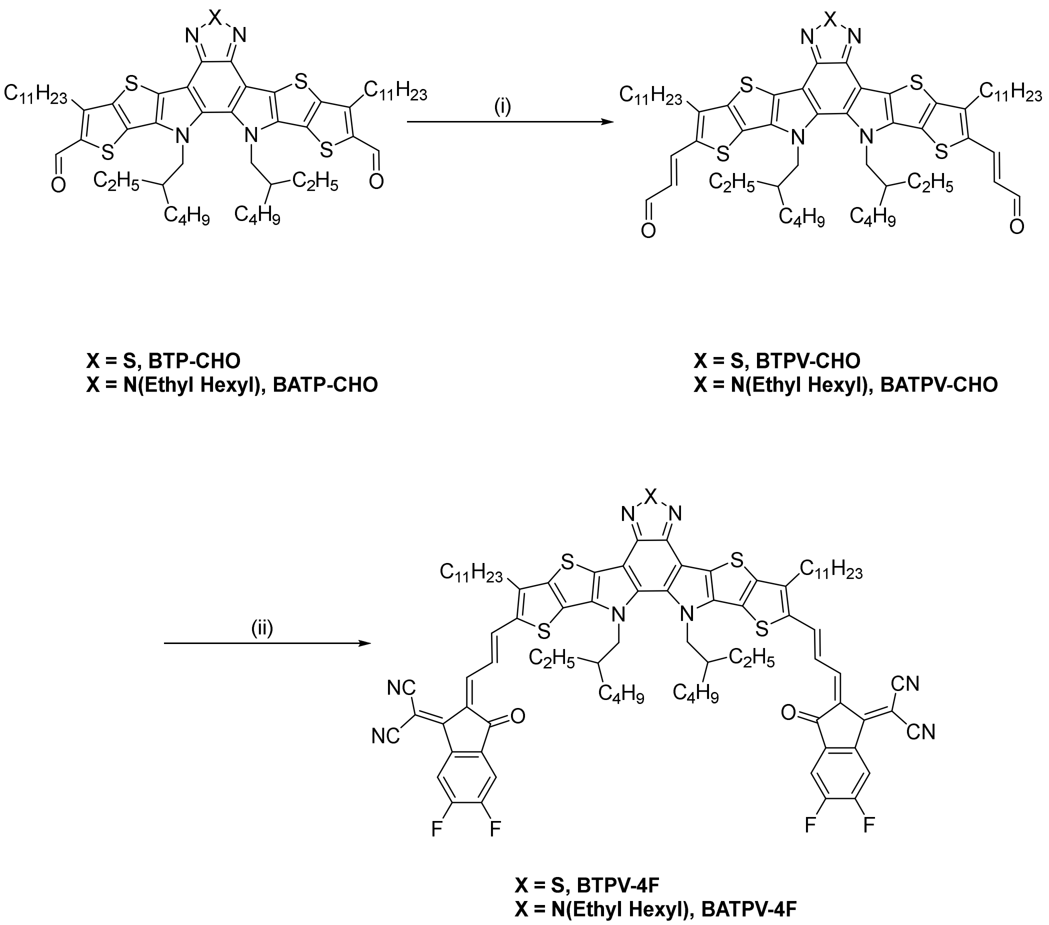

Scheme S1. Synthetic route of BTPV-4F and BATPV-4F. (i) (a) NaH, ((1,3-Dioxolan-2-yl)methyl)triphenylphosphonium bromide, THF 0 °C to RT, 4 h (b) 2N HCl, RT, 3 h. (ii) 2FIC, pyridine, $CHCl_3$, RT, 18 h.

Synthesis of BTPV-CHO:

A mixture of BTP-CHO (300 mg, 0.29 mmol) and ((1,3-dioxolan-2-yl)methyl) triphenylphosphonium bromide (150 mg, 0.35 mmol) in dry THF (20 mL) was cooled to 0 °C. NaH (60% in mineral oil, 35 mg, 0.88 mmol) was then added portionwise to the solution, and the reaction mixture was stirred at room temperature for 4 h. Upon completion of the reaction, 2 N HCl (10 mL) was added, and the mixture was stirred for an additional 3 h. The solvent was then removed under reduced pressure, and the residue was extracted with CH_2Cl_2, followed by sequential washing with water. The combined organic layers were dried over anhydrous $MgSO_4$, filtered, and concentrated. The crude product was purified by column chromatography (hexane/CH_2Cl_2 = 3:1) to afford BTPV-CHO as a red solid (220 mg, 70%). ^1H NMR (400 MHz, $CDCl_3$): δ 9.70 (d, J = 7.6 Hz, 2H), 7.78 (d, J = 15.3 Hz, 2H), 6.53 (dd, J = 15.2, 7.6 Hz, 2H), 4.61 (d, *J* = 7.8 Hz, 4H), 2.99 (t, *J* = 7.7 Hz, 4H), 2.05-1.96 (m, 2H), 1.91-1.81 (m, 4H), 1.52-1.21 (m, 35H), 1.12-0.84 (m, 23H), 0.74-0.55 (m, 12H). ^{13}C NMR (101 MHz, $CDCl_3$): δ 192.77, 147.71, 143.91, 142.91, 142.30, 137.08, 133.48, 132.68, 125.99, 125.49, 125.36, 112.38, 77.55, 77.23, 76.91, 55.28, 40.33, 32.10, 30.07, 29.89, 29.85, 29.81, 29.78, 29.75, 29.63, 29.53, 28.57, 27.78, 23.32, 22.88, 14.32, 13.89, 10.30. MS (HRFD) calcd. for $C_{62}H_{86}N_4O_2S_5$ [M$^+$]: *m/z*: 1078.53488, Found: 1078.53288.

Synthesis of BATPV-CHO:

This compound was prepared following the same method as that used for the synthesis of BTPV-CHO, using BATP-CHO as the starting material. Dark red solid. Yield: 58%. ^{1}H NMR (400 MHz, $CDCl_3$): δ 9.69 (d, *J* = 7.6 Hz, 2H), 7.77, (d, *J* = 15.2 Hz, 2H), 6.52 (dd, *J* = 15.2, 7.6 Hz, 2H), 4.73 (d, *J* = 7.2 Hz, 2H), 4.58 (d, *J* = 7.8 Hz, 4H), 2.98 (t, *J* = 7.8 Hz, 4H), 2.37 (quint, *J* = 6.2 Hz, 1H), 1.98-1.80 (m, 6H), 1.53-1.22 (m, 45H), 1.03-0.74 (m, 30H), 0.70-0.51 (m, 12H). ^{13}C NMR (101 MHz, $CDCl_3$) δ 192.80, 143.42, 143.13, 142.37, 137.17, 136.03, 133.04, 131.99, 125.84, 125.07, 124.80, 110.43, 77.55, 77.23, 76.91, 59.79, 55.06, 40.53, 40.29, 32.10, 30.63, 30.15, 29.93, 29.86, 29.81, 29.77, 29.67, 29.53, 28.60, 27.73, 27.64, 24.14, 23.42, 23.15, 22.89, 22.84, 22.81, 14.32, 14.22, 13.85, 13.83, 10.72, 10.40, 10.31. MS (HRFD) calcd. for $C_{70}H_{103}N_5O_2S_4$ [M$^+$]: *m/z*: 1173.69891, Found: 1173.69867.

Synthesis of BTPV-4F:

A mixture of BTPV-CHO (200 mg, 0.19 mmol) and 2-(5- or 6-difluoro-3-oxo-2,3-dihydro-1H-inden-1-ylidene)malononitrile (2FIC) (170 mg, 1.48 mmol) in $CHCl_3$ (20 mL) was treated with pyridine (0.5 mL) added dropwise. The reaction mixture was stirred at room temperature for 18 h. The solvent was then removed under reduced pressure, and the residue was purified by column chromatography (hexane/ CH_2Cl_2 = 1:1) to afford BTPV-4F as a black solid. (220 mg, 79%). ^{1}H NMR (400 MHz, $CDCl_3$): δ 8.69-8.43 (m, 6H), 7.79-7.61 (m, 4H), 4.67 (d, *J* = 8.2 Hz, 4H), 3.01 (t, *J* = 7.9 Hz, 4H), 2.16-2.02 (m, 2H), 1.92-1.79 (m, 4H), 1.52-1.21 (m, 32H), 1.16-0.84 (m, 22H), 0.78-0.64 (m, 12H). ^{13}C NMR (101 MHz, $CDCl_3$): δ 187.46, 157.61, 147.67, 147.06, 145.36, 145.26, 144.56, 137.87, 137.18, 136.81, 135.07, 132.96, 128.02, 123.54, 122.38, 115.25, 115.04, 114.58, 113.33, 112.71, 112.53, 77.55, 77.23, 76.91, 69.56, 55.53, 40.31, 32.11, 30.39, 29.95, 29.84, 29.82, 29.75, 29.67, 29.54, 28.85, 27.87, 23.38, 22.96, 22.89, 14.32, 13.94, 10.46. MS (HRFD) calcd. for $C_{86}H_{90}F_4N_8O_2S_5$ [M$^+$]: *m/z*: 1502.57209, Found: 1502.57066.

Synthesis of BATPV-4F:

This compound was prepared following the same method as that used for the synthesis of BTPV-4F, using BATPV-CHO as the starting material. Black solid. Yield: 66%. ^{1}H NMR (400 MHz, $CDCl_3$): δ 8.66-8.38 (m, 6H), 7.94-7.56 (m, 4H), 4.79-4.53 (m, 6H), 3.14-2.86 (m, 4H), 2.40-2.33 (m, 1H), 2.05-1.98 (m, 2H), 1.91-1.80 (m, 4H), 1.52-1.20 (m, 45H), 1.07-0.82 (m, 31H), 0.76-0.57 (m, 12H). ^{13}C NMR (101 MHz, $CDCl_3$): δ 187.44, 155.92, 155.78, 153.31, 153.17, 136.83, 135.07, 129.10, 127.07, 115.13, 114.92, 112.63, 112.45, 77.55, 77.23, 76.91, 59.88, 55.41, 40.53, 40.21, 32.11, 30.62, 29.99, 29.84, 29.82, 29.76, 29.70, 29.53, 28.97, 28.57, 27.74, 24.14, 23.42, 23.15, 22.89, 14.32, 14.23, 13.87, 10.72, 10.48. MS (HRFD) calcd. for $C_{94}H_{107}F_4N_9O_2S_4$ [M^+]: *m/z*: 1597.73612, Found: 1597.73596.

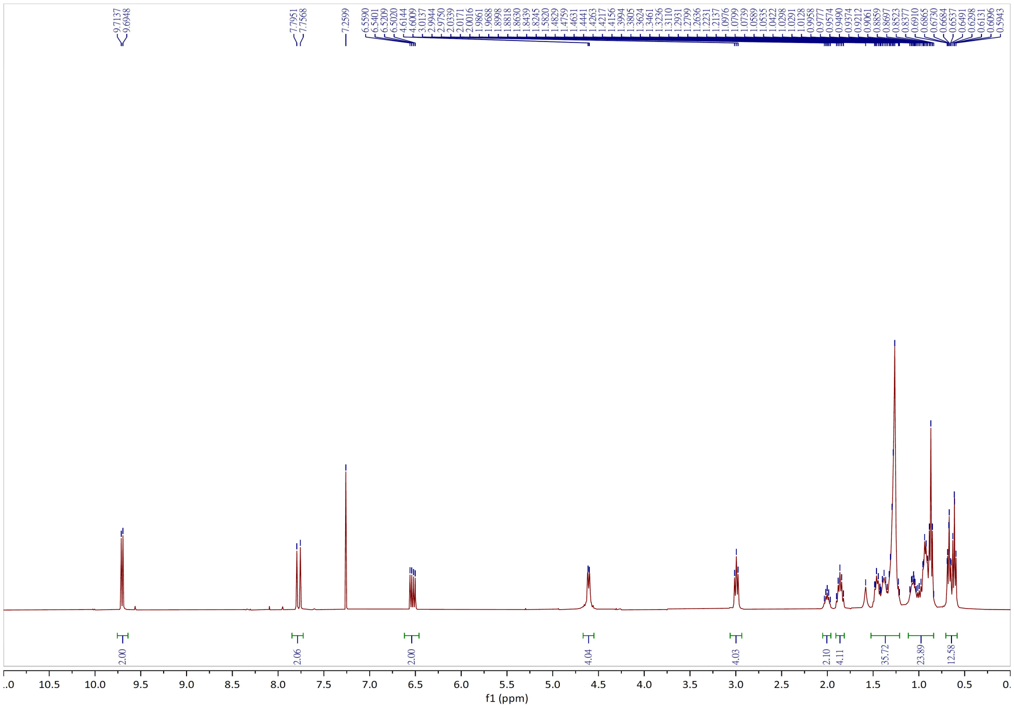

Fig. S18. ^{1}H NMR (400 MHz) of **BTPV-CHO** in CDCl$_3$.

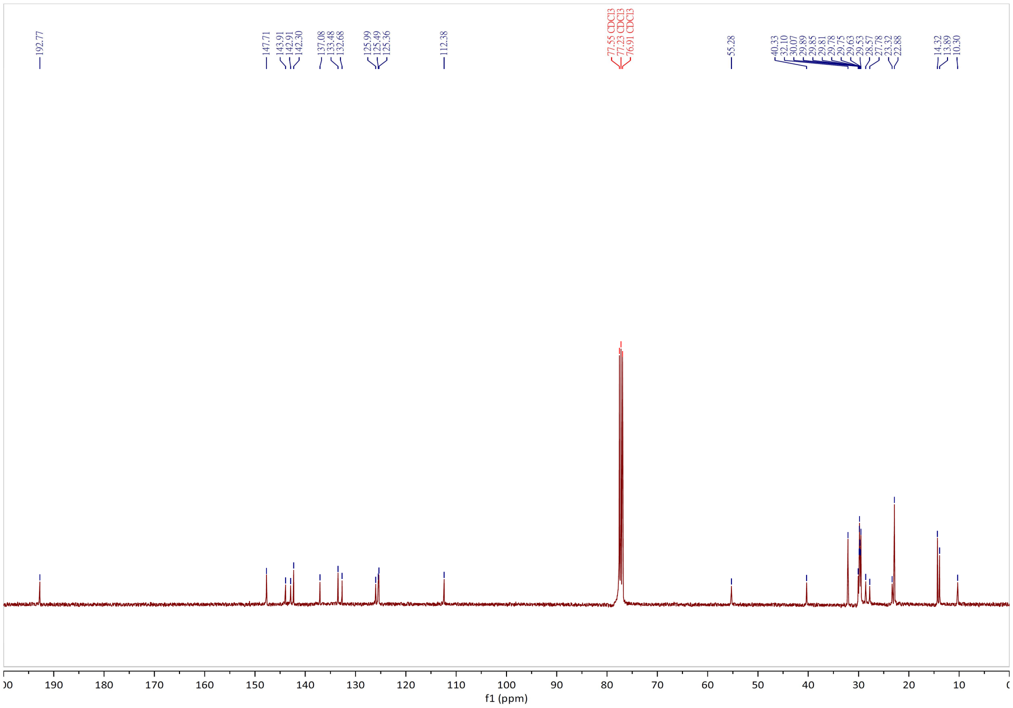

Fig. S19. ^{13}C NMR (101 MHz) of **BTPV-CHO** in CDCl$_3$.

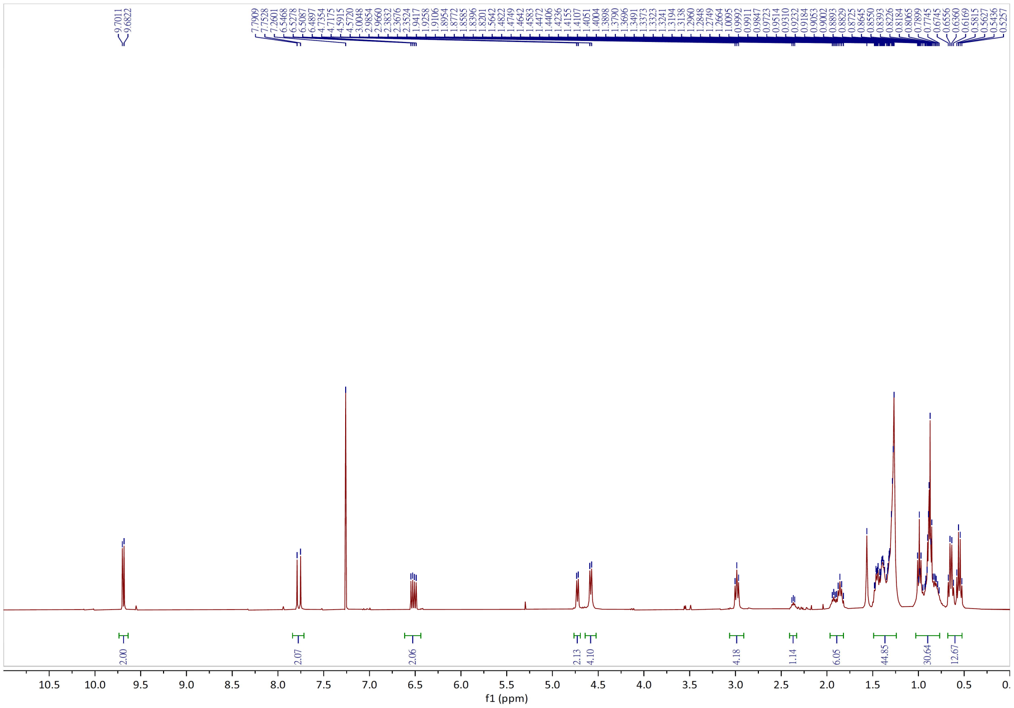

Fig. S20. ^{1}H NMR (400 MHz) of **BATPV-CHO** in $CDCl_3$.

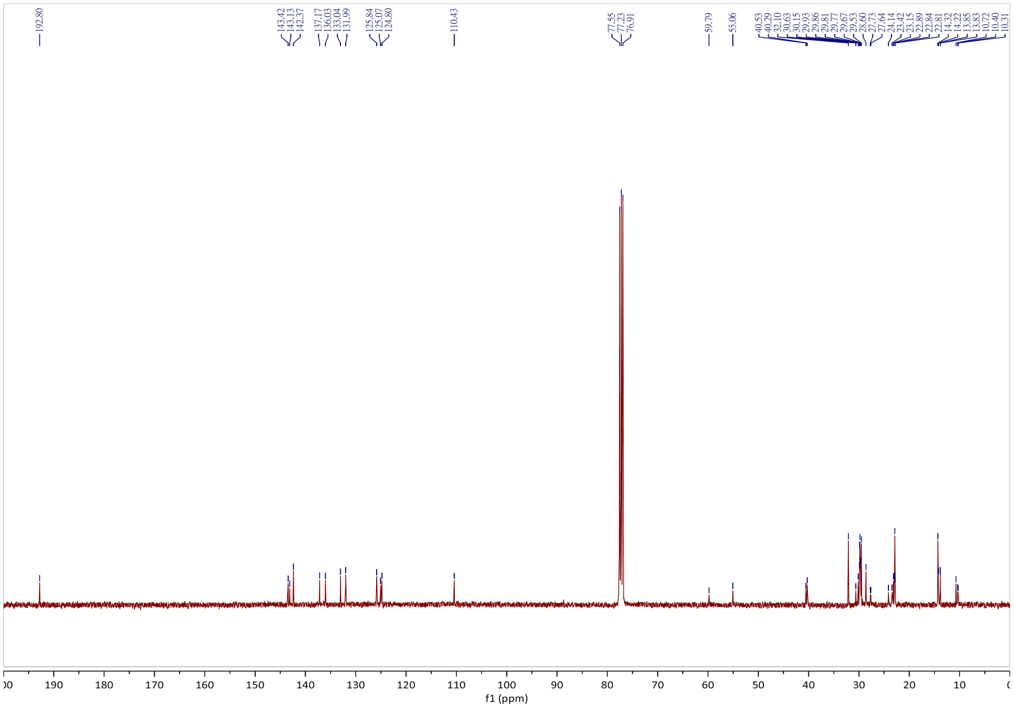

Fig. S21. ^{13}C NMR (101 MHz) of **BATPV-CHO** in $CDCl_3$.

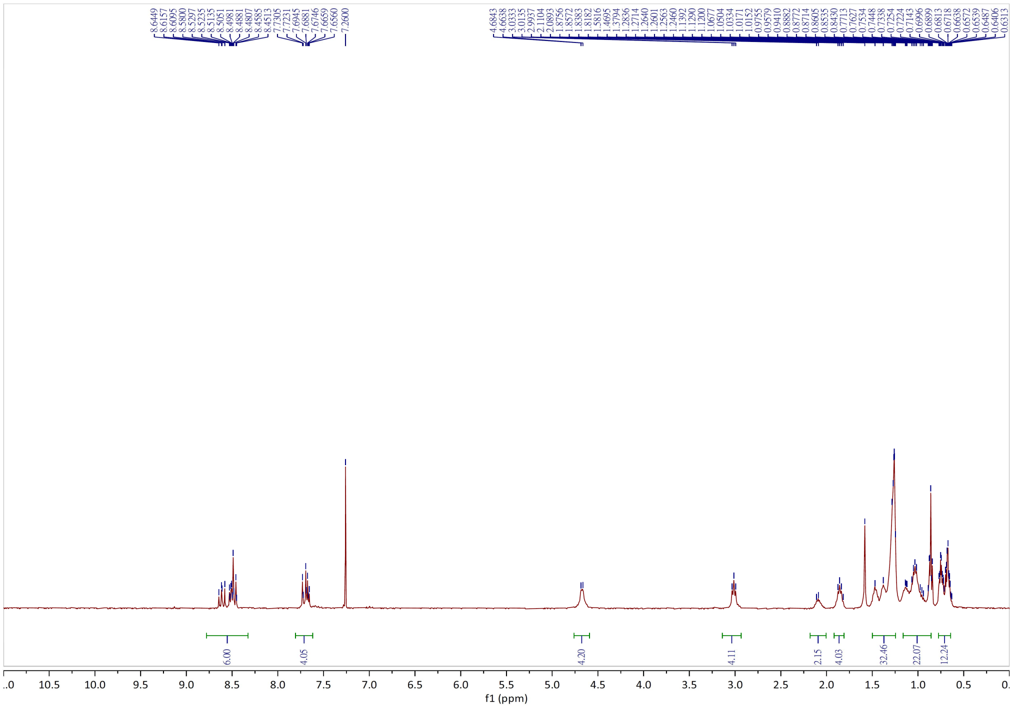

Fig. S22. ^{1}H NMR (400 MHz) of **BTPV-4F** in $CDCl_3$.

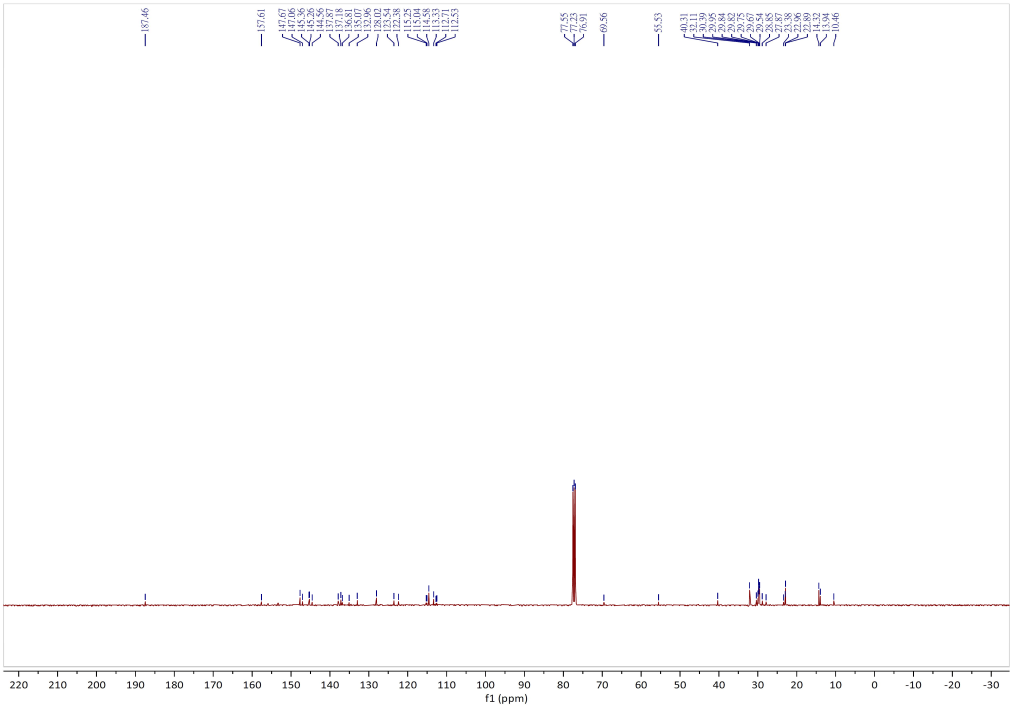

Fig. S23. ^{13}C NMR (101 MHz) of **BTPV-4F** in $CDCl_3$.

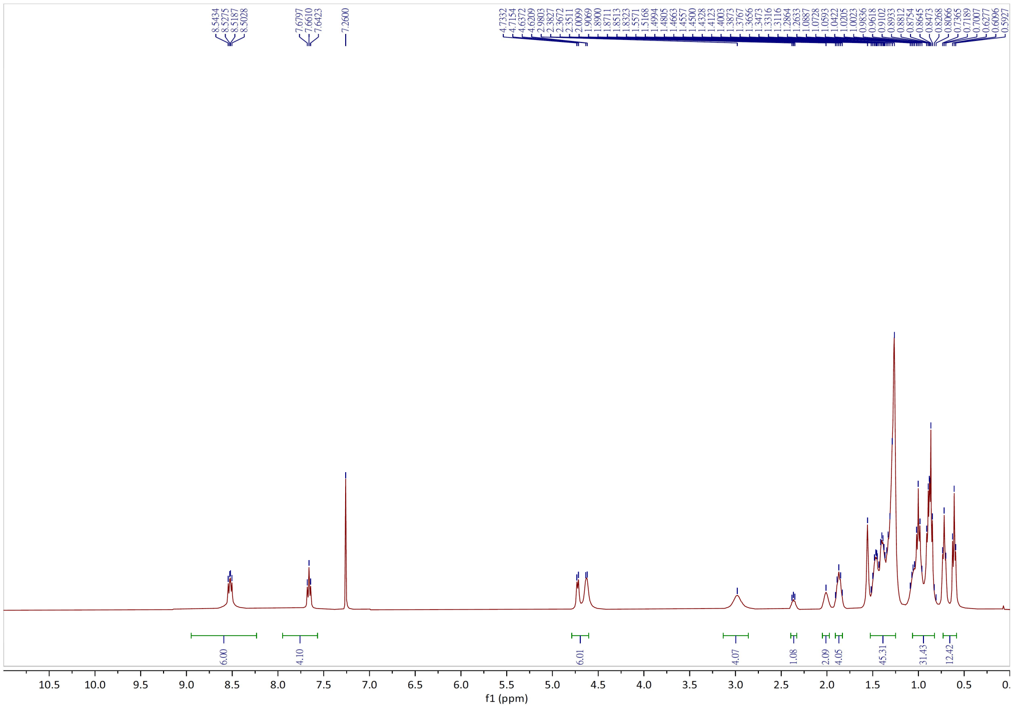

Fig. S24. ^{1}H NMR (400 MHz) of **BATPV-4F** in $CDCl_3$.

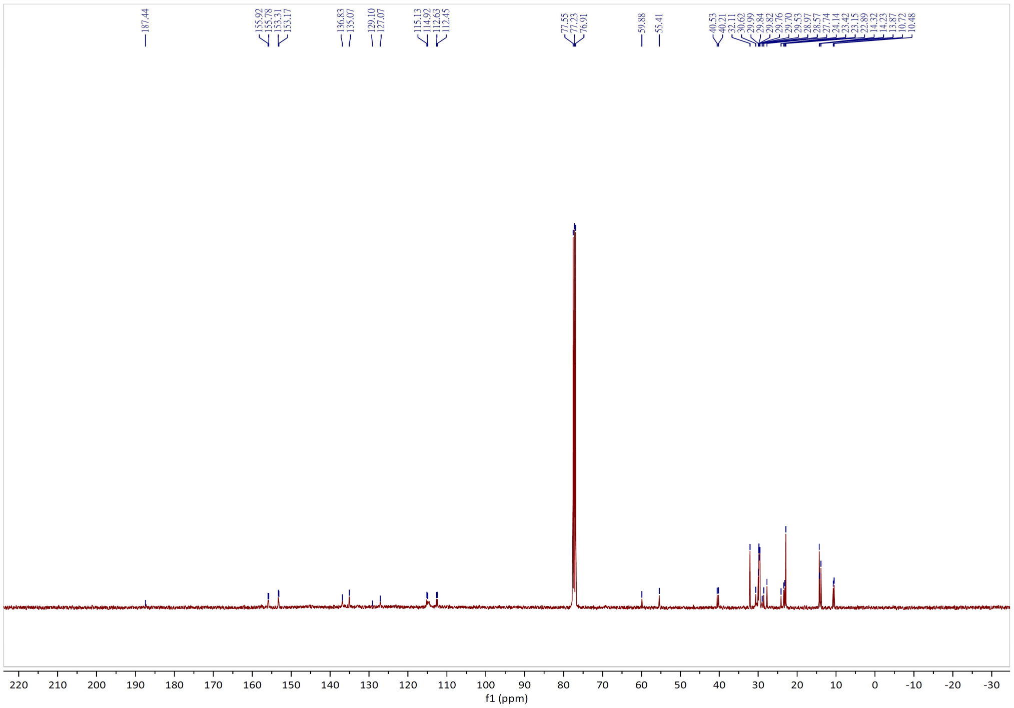

Fig. S25. ^{13}C NMR (101 MHz) of **BATPV-4F** in $CDCl_3$.